Computationally Efficient Models of Flow-through Affinity-based Assays

D. Kent Peterson, William H. Wright, D. Brent MacQueen*

* SRI International, 333 Ravenswood Ave., Menlo Park, CA 94025, kent.peterson@sri.com

ABSTRACT

We present a new paradigm for modeling, simulation, and optimal design of biosensors, based on an innovative, computationally efficient formulation. Here we illustrate the approach on the design of flow-through affinity-based (a.k.a. lateral flow) bioassays. We briefly discuss the mathematical and computational models and present an example of parameter optimization and performance tradeoffs.

Keywords: scaling model, microfluidic, convex programming, lateral flow assay, microfabricated

1 INTRODUCTION

Lateral flow strips are a common assay format used in a variety of applications, including home pregnancy testing, clinical point-of-care screening for HIV, agribusiness surety against pathogens, and military bioagent detection. Current lateral flow assays are fabricated with a porous wick material, such as nitrocellulose paper. The random microstructure of these substrates presents difficulties for assay optimization and causes undesirably large coefficients of variation in assay results.

We have developed a new substrate material to replace the paper strip. The material is a micro-machined porous structure (μMaPS) whose microstructure can be designed and fabricated to desired dimensions. An example strip is shown in Figure 1. Preliminary results of an hCG assay are shown in Figure 1.

The deterministic and precisely engineered dimensions of μMaPS substrates present the opportunity to optimize their design by controlling the surface-to-volume ratio, total capture surface area, depletion layer thickness, capture fraction, and spatial variation of these properties. Optimally designed μMaPS can overcome the serious shortcomings of random porous media currently used in lateral flow assays.

We have developed computationally efficient models of μMaPS that enable simulation, analysis, and rational optimization of an assay's performance. These models represent the phenomenology of micro- and nanoscale physico-chemical processes, including flow through the microstructures, surface binding of analytes and reporters, and optical transduction mechanisms, as well as manufacturing and cost constraints. The models are mathematically convex, allowing efficient optimization by convex programming algorithms.

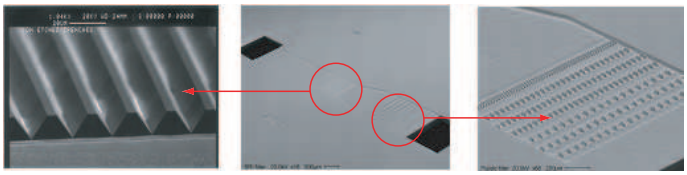

Figure 1: Micrographs of the microfabricated substrate (b). Capture zone troughs (a) are 14 μm deep, 1 mm long, and spaced at a 25 μm pitch. The microstructured filter (c) comprises anisotropically etched bumps at three pitches to trap debris before entering the capture zone (left). Image magnifications are (a) 1000×, (b) 16×, (c) 68×.

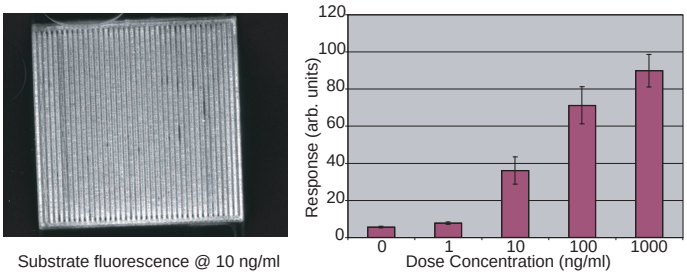

Figure 2: Dose response of hydrostatic hCG assay performed in a V-groove microchannel with a PE reporter.

2 MICROFABRICATED WICKS

Our microfabricated substrates are prepared from silicon wafers using standard semiconductor industry processing protocols. The size and location of the microstructures were determined by the intended use of the device. We expected the device to be used to capture and detect targets ranging in size from nanoscale peptides to microscale bacteria.

The device shown in Figure 1 was fabricated with triangular (V-shaped) anisotropically etched channels having a vertex angle of 70°. Channels were fabricated in silicon using a KOH etch to a depth of 14 μm on a 1 mm×1 mm planform with 25 μm pitch ($\sim$ 5 μm separates adjacent channels at the surface).

In Section 3 we present our models for μMaPS, and in Section 4 discuss an optimal design tradeoff study, based on these models.

3 MATHEMATICAL MODELS

Our present models are derived from fundamental physical parameters (e.g., fluid viscosity). It is possible (and desirable) to augment the models with laboratory measurements (e.g., observed scaling laws); however, laboratory validation of the models, simulations, and optimization predictions is yet to be done.

Our mathematical models of μMaPS represent the three key physico-chemical aspects of the device:

- Microfluidics: flow through the microchannels
- Capture: binding of the analyte at the channel surface by specific antibody-antigen recognition
- Signal transduction: of the labeled analyte

If possible, we wish to express these models in a mathematically convex form, allowing optimization by highly efficient convex programming algorithms. The models are connected in a cascade: Driving pressure $\Rightarrow$ Flow rate $\Rightarrow$ Capture fraction $\Rightarrow$ Signal level.

3.1 Flow Rate

At the flow rates and channel dimensions we are considering, the microfluidic flow is laminar. The mean flow rate ($\overline{u}$) is proportional to the square root of the driving pressure (p) through a relationship involving the coefficient of friction (C_f), the hydraulic diameter (d_h) and the channel length (L):

$$\Delta p = C_f \frac{4L}{d_h} \rho \overline{u}^2/2$$

$$C_f \propto 1/N_{Re}$$

$$\overline{u} = \int\int dS u_z / \int\int dS$$

$$d_h = \frac{\text{Area}}{\text{Perimeter}/4}$$

$$N_{Re} = \overline{u} w/\nu$$

$$\nabla^2 u_z(x,y) = \frac{\Delta p}{\mu L}$$

where non-dimensional quantities for several simple channel cross sections are given in Table 1. N_{Re} and N_{Sh} are the Reynolds number and the Sherwood number of the flow, respectively [1, p. 75ff].

At the entrance to the channel, the flow is uniform. As it continues down the confines of the channel, the boundary layer thickens until it grows to the centerline and entirely supplants the undisturbed core flow.

Table 1: Normalized parameters for various sections

	triangle	square	circle	sheet
d_h/w	.577	1	1	2
C_f/N_{Re}	13.3	14.2	16	24
N^0_{Sh}	2.35	2.89	3.66	7.54

The entrance length, defined as the distance over which this transition occurs, is given approximately as $X = 0.01 w N_{Re}$. Beyond the entrance length, the transverse flow profile is fully developed and does not change. For flow in microfabricated channels, where $N_{Re} \ll 100$, the entrance length is less than the channel diameter and, to excellent approximation, we can assume that the channel flow is everywhere fully developed.

3.2 Capture Fraction

Not all of the analyte flowing through the channels is captured (i.e., bound by the antibodies) at the surface. Only that analyte within the diffusion boundary layer can be adsorbed and, because the flow is laminar and not mixed, the only mechanism for transport from the bulk flow to the boundary layer is diffusion. We will assume that all analyte that reaches the walls is captured and that none dissociates after capture (tantamount to assuming that the equilibrium constant for antibody-antigen dissociation is negligibly small). Under these conditions the mass transport toward and capture at the wall is analogous to energy (heat) transport in a pipe, the boundary condition being zero concentration (analogously, temperature) at the wall. This analogy is satisfactory as long as the surface functionalization (antibodies here) is not saturated by antigen binding. Referring to the extensive literature on heat flow through pipes,[1, p. 89ff], [2, Ch. 9], [3, p. 105ff] we express the capture fraction (f_c) as the flux at the wall ($\hat{J}$), which is an integral of an expression in the local Sherwood number (N_{Sh}) along the normalized distance down the pipe (ζ):

$$f_c = \hat{J}\left(\frac{z}{w N_{Pe}}\right) \quad \text{, where} \quad N_{Re} = \overline{u} w/D$$

$$\hat{J}(\zeta) = \int_0^{\zeta} d\zeta' N_{Sh}(\zeta') \exp\left(-\int_0^{\zeta'} d\zeta'' N_{Sh}(\zeta'')\right)$$

$$N_{Sh}(\zeta) = \begin{cases} N^1_{Sh}\zeta^{-1/3} & , \ \zeta \le 0.05 \\ N^0_{Sh} & , \ \zeta > 0.05 \end{cases}$$

Figure 3.2 shows a plot of the local Sherwood number and the integrated capture fraction as a function of ζ.[1]

[1]The solid lines show the results for a constant boundary value (antibody surface density). For comparison, the dashed blue line shows the Sherwood number for a constant boundary flux (antigen capture rate). The two profiles are qualitatively similar (i.e., both are concave, with the same asymptotic scaling exponents).

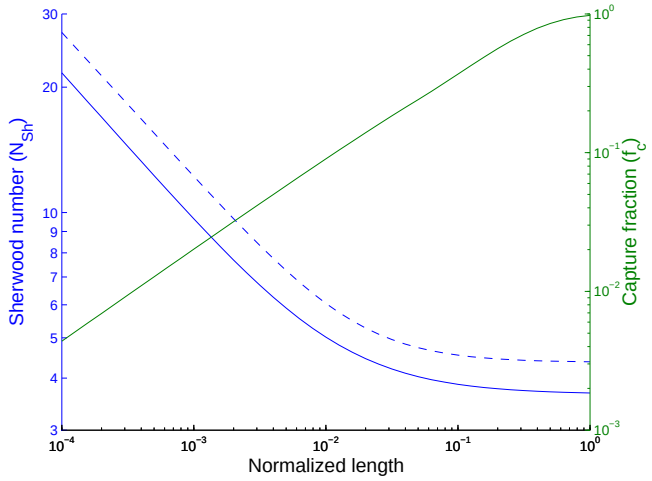

Figure 3: Sherwood number (N_{Sh}) and capture fraction (f_c) versus normalized channel length (ζ)

Just as with momentum transport (drag), the transport of mass (analytes) or energy (heat) exhibits an entrance region over which the transverse concentration transitions from a uniform profile at the entrance to a fully developed profile further down the channel. While the hydrodynamic entrance region is inconsequential in microfluidic channels, the developing region for diffusion can extend many channel diameters streamwise (typical Peclet numbers are on the order of 10^7), so we cannot assume that the channel diffusion is fully developed.

In the developing region, the Sherwood number is proportional to $\zeta^{1/3}$. Consequently, the wall flux grows as $z^{2/3}$. This scaling behavior has been confirmed by numerical simulation of mass transport in microfluidic flows in rectangular cross-section channels [4].

3.3 Transduction, Geometry, and Cost

We use a very simple model for signal transduction: the signal is assumed to be proportional to the concentration of analyte in the sample (c_0) times the capture fraction at the walls (f_c) times the flux (which is equal to the channel cross section area (A_{cs}) times the duration of the assay (t_f)). The signal is assumed to be corrupted by two noise components: a constant background noise (n_{bg}), e.g., from the optical detector system; and nonspecifically bound label (n_{nsb}), which is proportional to the assay duration (t_f):

$$S = c_0 f_c \overline{u} A_{cs} t_f \ , \quad N = n_{bg} + n_{nsb} \ , \quad t_f = V_0 / \overline{u} A_{cs}$$

Figure 3.3 shows the growth of signal and noise as a function of assay development time. The minimum detectable analyte concentration (c_{min}) is given in terms of a minimum signal-to-noise ratio (SNR_{min}) required for detection.

$$c_{min} = \frac{N \cdot SNR_{min}}{f_c \overline{u} A_{cs} t_f}$$

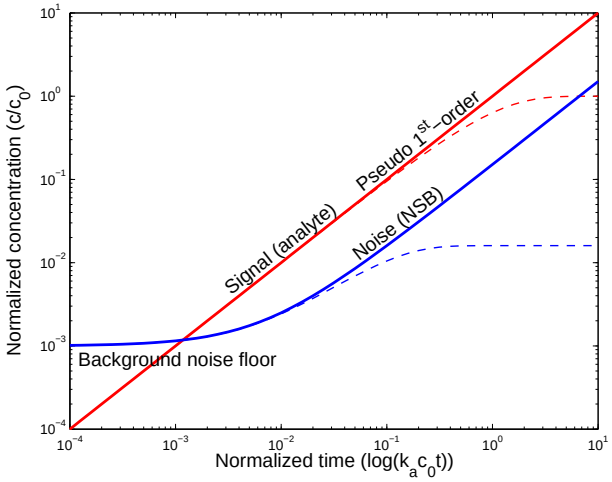

Figure 4: Specific and nonspecific capture vs. time. The present model (solid lines) assumes pseudo-first-order kinetics, ignoring the effects of saturation and backreaction (dashed lines).

The geometry of the microchannel capture zone is described by the simple scaling laws $A_{cs} \propto mw^2$, $A_{surf} \propto mwL$, and $A_{subs} \propto mwL$, where m is the number of parallel channels, w is their width, and L is their length.

A notional fabrication cost is expressed as the sum of three terms: a fixed cost (e.g., for tooling); a cost proportional to device area (e.g., the cost of the substrate material); and a cost for the surface area (e.g., cost of antibody and linker reagents):

$$\$_{tot} = \$_{fixed} + \$_{subs} A_{subs} + \$_{surf} A_{surf}$$

where $\$_{fixed}$, $\$_{subs}$, $\$_{surf}$ are proportionality constants.

The total cost ($\$_{tot}$) and limit of detection (c_{min}) are employed in the optimization of the device as objective or constraint functions.

4 COMPUTATIONAL MODELS

4.1 Optimization

Optimization of the assay could take many forms. In general, one would seek to optimize (minimize or maximize) some performance or cost metric while satisfying applicable constraints to a feasible region of the design space. In this section, we illustrate an example optimization problem: Find the optimal values for the channel design parameters (number, width, and length) and driving pressure that will give the smallest detectable analyte concentration (i.e., smallest limit of detection, or LOD), subject to constraints on the channel dimensions (e.g., because of microfabrication process limitations), the operating flow velocity ($\overline{u}$), driving pressure (p), and assay development time (t_f). Figure 4.1 shows a dependency graph—the functional relationships among

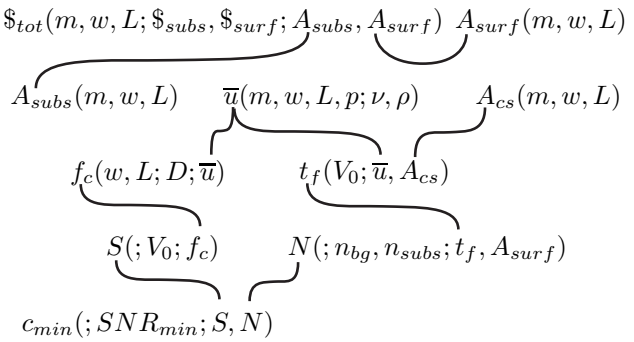

Figure 5: Dependency graph for design variables (m, w, L, p), parameters $(\nu, \rho, V_0, D, \$_{subs}, \$_{surf}, n_{bg}, n_{subs}, SNR_{min})$, and models $(\overline{u}, \$_{tot}, A_{subs}, A_{cs}, A_{surf}, f_c, t_f, S, N, c_{min})$.

Table 2: Parameter values used in optimization example

Param	Value	Param	Value
W_{max}	10 mm	V_0	1 μL
L_{max}	10 mm	T_{max}	1000 sec
n_{nsb}	10^2 part/mm^2/s	SNR_{min}	2
$\$_{fixed}$	\$0.10	n_{bg}	10^4 part
$\$_{surf}$	\$0.001/mm^2	$\$_{subs}$	\$0.001/mm^2
$\$_{max}$	\$1.00	U_{max}	100 mm/sec
D	7×10^{-12}m^2/s	P_{max}	100 kPa
ρ	10^3 kg/m^3	ν	10^-6 m^2/s

all of the parameters and variables—for all of the models discussed in the earlier sections.[2]

The statements in Figure 4.1 together make up a mathematical program that can be solved by any of various methods. To demonstrate this model-based optimization, we solved the program in Figure 4.1 with the parameter values shown in Table 2.

4.2 Parameter Sensitivity and Performance Tradeoffs

The model-based optimization framework enables more than an optimal design. It allows the designer to explore tradeoffs in the design space. Figure 4.2 shows a graphical example. The red symbols indicate optimal performance (minimum detectable analyte concentration, c_{min}) for a particular choice of a design parameter (maximum assay development time, T_{max}). The straight

[2]We have endeavored to construct the individual models as convex functions, but do not explicitly exploit that convexity here. Convexity of the individual models is necessary, but not sufficient, to guarantee that the overall mathematical program is convex. Composition of convex functions [e.g., $f(g(x))$] is not necessarily convex. We have not yet proven that the compositions, indicated in the dependency graph shown in Figure 4.1, are all convex. This is required before we can apply convex optimization methods to the assay optimization problem. Therefore, in the work reported here, we have used the general constrained nonlinear optimization algorithm *fmincon* in Matlab's optimization toolbox.

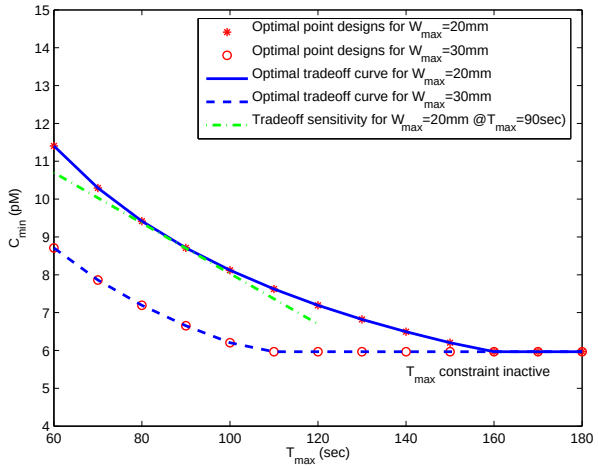

Figure 6: Illustration of tradeoff analysis: minimum detectable analyte concentration (c_{min}) versus the maximum development time constraint (T_{max})

dashed green line shows the local sensitivity of the performance to small variations in the design parameter and the blue curves show the optimal tradeoff in performance with variation of the maximum-time constraint for two different values of the maximum device width constraint (W_{max}). The same analysis can be done with N design parameters, giving an N-dimensional optimal tradeoff surface. Computing the tradeoff surface requires the solution of many optimal designs, placing a premium on efficient optimization methods, hence our predilection for convex model parameterizations.

Acknowledgment: The modeling work and portions of the microfabrication work were funded by DARPA's SimBioSys program. This paper is approved by DARPA for public release with unlimited distribution.

REFERENCES

[1] Bejan, Adrian, Convection Heat Transfer, Wiley-Interscience, McGraw-Hill, 1984.
[2] Deen, William M., Analysis of Transport Phenomena, Oxford University Press, 1998.
[3] Shah, R.K., London, A.L., Laminar Flow Forced Convection in Ducts, Academic Press, 1978.
[4] Carson, Larry, personal communication.